PAPER

Structural evolution and effective improvement of emission quantum yields for silicon nanocrystals synthesized by femtosecond laser ablation in HF-contained solution

IOP Publishing Nanotechnology
Nanotechnology 30 (2019) 015705 (11pp) https://doi.org/10.1088/1361-6528/aae67c

Structural evolution and effective improvement of emission quantum yields for silicon nanocrystals synthesized by femtosecond laser ablation in HF-contained solution

Jianjun Wang[1], Yingxiong Zhang[1], Huilian Hao[1,3] and Wenzhong Shen[2,3]

[1] College of Material Engineering, Shanghai University of Engineering Science, 333 Long Teng Road, Shanghai 201620, People's Republic of China
[2] Institute of Solar Energy, and Key Laboratory of Artificial Structures and Quantum Control (Ministry of Education), Department of Physics and Astronomy, Shanghai Jiao Tong University, 800 Dong Chuan Road, Shanghai 200240, People's Republic of China

E-mail: sulee8866@126.com and wzshen@sjtu.edu.cn

Received 9 July 2018, revised 26 September 2018
Accepted for publication 5 October 2018
Published 26 October 2018

Abstract

Stable luminescent colloidal silicon (Si) nanocrystals (NCs) with sufficient surface protection are prepared through femtosecond laser ablation in organic solvent containing diverse concentrations of HF solution. The average size of Si NCs shows the decreasing tendency from 6.5 to 2.7 nm when the concentration of HF varies from 0 to 11.1 vol% (volume ratio). In line with the structural evolution, UV–visible absorption, photoluminescence (PL) excitation spectra, and time-resolved PL, we propose that room temperature blue emission peaks at 412 and 440 nm originate from alkyl-related radiative recombination centers. The enhanced PL quantum yield of colloidal Si NCs from 16.3% to 76.5% has been attributed to the effective passivation and suppression of non-radiative defect centers with increasing HF concentration from 0 to 11.1 vol%.

Keywords: colloidal silicon nanocrystals, emission quantum yield, femtosecond laser ablation

(Some figures may appear in colour only in the online journal)

Ever since the luminescence emitted from silicon (Si) nanocrystals (NCs) was reported for the first time in 1990 [1], quantum-scale Si NCs have been considered as promising luminous materials with adjustable emission color and environmental friendliness properties. Recently, based on the low-cost, simplified operation by solution-supported technology [2], colloidal NCs have received extensive attention in photoelectric and biotic applications, for instance photodetectors [3], luminous diodes [4], solar cells [5] and bioimaging tools [6]. To control the photoelectric properties and chemical reactivity of colloidal Si NCs within these applications, it is necessary to develop the surface functionalization of Si NCs [7]. Many effective organic ligands such as hydride [8] and halogen [9] groups have been applied to Si nanomaterials. However, easily oxidized and kinetically labile properties for hydride and halogen passivation lead to the relatively low photoluminescence (PL) quantum yields (QYs). It is reported that alkyl groups terminated on the Si NCs surface ensure colloidal stability and minimize oxidation which is detrimental to optical and electronic properties, without showing degradations in ambient air [10]. Therefore, it is important to modify Si NCs surface by alkyl groups.

[3] Authors to whom any correspondence should be addressed.

Owing to the advantageous solution properties and stability, styrene has been a preferred choice for Si NCs surface functionalization [11, 12].

There are various techniques for fabricating colloidal Si NCs with alkyl termination, such as plasma enhanced chemical vapor deposition of silane [13], hydrosilylation [14], and wet-chemical synthesis [15]. It has been proved that the technology of laser irradiation in solution is a one-step process to fabricate alkyl-terminated colloidal Si NCs [16]. The Si targets are irradiated under a high power laser irradiation so that the fragmentation processes efficiently take place, leading to the generation of Si NCs. Simultaneously, the surfaces of colloidal Si NCs are terminated by alkyl groups through the effective reactions between the reactive solution and NCs [16]. Alkyl termination on the surface can refrain colloidal Si NCs from agglomeration via steric barriers or electrostatic repulsion, and ensure the high dispersibility and stability in solution. The PL QYs of laser irradiation in liquid process is relatively lower (∼10%–25%) [17, 18] than those prepared by other methods. Miyano *et al* [19] have reported that the high PL quantum yield (PL QY, 55%) has been promoted by the combination of hydrosilylation procedure with photo-initiated reaction under UV irradiation. Mangolini *et al* [20] and Jurbergs *et al* [21] have discovered that high PL QYs have exceeded 60% from plasma-based synthesis. Besides, Li *et al* [22] have reported that the strongly enhanced fluorescence with PL QYs up to 75% for Si NCs after a novel surface modification have been obtained. By comparison, it has become a challenge to improve the PL QYs of alkyl-passivated Si NCs fabricated by laser irradiation in liquid environment. It is reported that the PL intensity of Si NCs is generally restricted by non-radiative recombination of excitons. The P_b defect centers, which act as non-radiative recombination centers, are found to reside at the Si/SiO_2 interface layers, leading to relatively low luminescence intensity [23]. Therefore, it is necessary to lessen the P_b defect centers to enhance PL QYs.

We have recently published the work [24], which mainly focuses on the effect of the laser ablation time (LAT) on the micro-structure and optical properties. It is found that, with increasing LAT from 30 to 120 min, the size of the prepared colloidal Si NCs decreases from ∼4.2 to 1.4 nm, the corresponding PL QY enhances from 23.6% to 55.8%. The surfaces of prepared colloidal Si NCs have been well passivated by carbon chains and partly oxidized as confirmed by FTIR and XPS measurements. The blue PL bands at 405 and 430 nm have been assigned to the electron–hole pair recombination associated with Si–C–H_2 and Si–O–Si vibration phonons, respectively.

However, on the one hand, laser ablation in the organic solvent in preparing alkyl-terminated colloidal Si NCs usually makes its size distribution wider, and the productivity is relatively low due to the uses of high power pulsed laser. On the other hand, the presence of oxidization layers can result in the degradation of PL from Si NCs, which further leads to the decrement of the PL QYs. This influence is a severe problem for light-emitting devices and bio-imaging applications. Thus, it is urgent to improve the QY of alkyl-terminated Si NCs prepared by laser irradiation method to meet the need of optoelectronics devices applications.

In this work, we investigate the significant effect of HF etching on the structural transformation, PL properties, and significant improvement of PL QYs for colloidal Si NCs. It is clearly found that the average sizes and PL QYs of Si NCs are dependent on HF concentration for laser irradiation in HF-contained organic solution. The size distribution of the prepared colloidal Si NCs varies from ∼6.5 to 2.7 nm with increasing HF concentration from 0 to 11.1 vol% (volume ratio) and the measured PL QY is found to enhance from 16.3% to 76.5% with increasing HF concentration. The influence of surface trap states on the PL behavior adds the complexity of accurate interpretation, the underlying mechanism of the prepared Si NCs with the bright blue luminescence is discussed as well. It is considered that alkyl-related radiative recombination centers are introduced to initiate the blue emission. The advanced method of laser ablation technique in liquid containing HF provides a simple, flexible and inexpensive way for preparation of high-quality colloidal Si NCs.

The obtained colloidal Si NCs were fabricated by femtosecond (fs) laser ablation as discussed in a previous procedure [25]. Briefly, porous Si powder (80 mg, Aladdin), styrene (>99%, 10 ml, Aladdin) and a diverse amount of HF acid solution were mixed in the quartz cuvette, respectively, acting as the target materials. The laser beam was focused on the target materials by performing a Ti:sapphire fs laser (worked with 800 nm wavelength, 100 fs pulse width, 80 MHz frequency and 0.15 mJ cm^{-2} laser fluence, respectively). During the fs laser ablation, magnetic stirrer was used to continuously stir the reactive solution. The fabricated colloids samples were named as S_x ($x = 1$, 2, 3, and 4) with corresponding HF concentration = 0, 3.0, 5.9, and 11.1 vol%, respectively. After finishing fs laser ablation for 2 h, the prepared solution was firstly centrifuged at 12 000 rpm for 1 h and then the supernatant liquid was collected by a membrane filter with around 200 nm of each pore size so as to get the colloidal solution for the following structure and optical properties measurements.

The structural properties including the generation and morphology of the obtained colloidal Si NCs were analyzed by high resolution transmission electron microscopy (HRTEM, JEOL JEM-2100F) and microprobe Raman spectra measurements (Renishaw, inVia-Reflex), respectively. The terminal chemical bonding construction of the colloids was investigated by using a Fourier transform infrared (FTIR) spectrometer (ThermoFisher, Nicolet 6700) within the 400–4000 cm^{-1} range. X-ray photoelectron spectroscopy (XPS) spectra (ThermoFisher, ESCALAB 250 XI) was employed to analyze the bonding configurations. Electronic spin resonance (ESR) measurements were performed with an X-band spectrometer (Bruker, about 20.65 GHz) at room temperature. UV–visible (UV–vis) absorption measurements were carried out using a Perkin-Elmer Lambda 35 spectrometer. Room temperature PL and PL excitation (PLE) spectra were monitored via a Hitachi High-Technologies F-7000 fluorescence spectrophotometer. The PL decay curves were measured by using a 405 nm diode

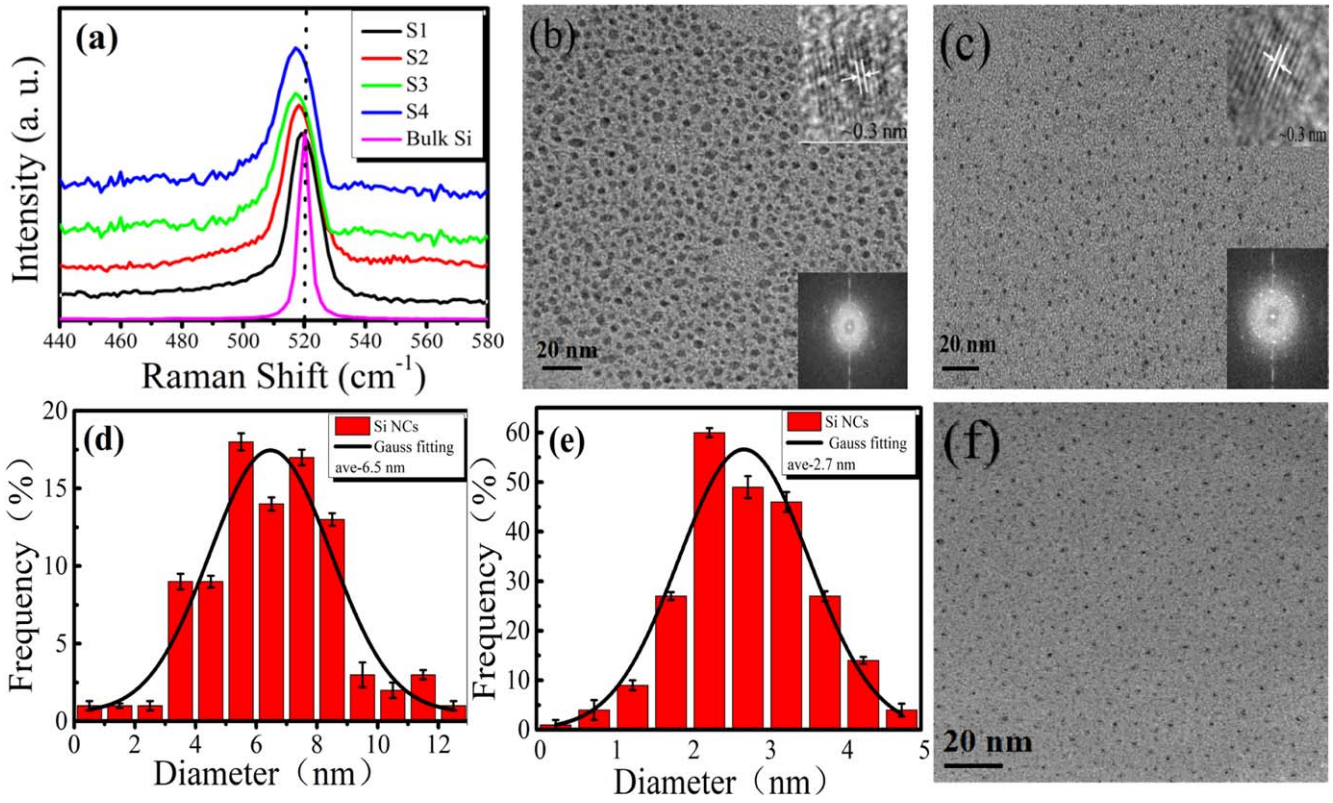

Figure 1. (a) Room temperature Raman spectra of all the samples produced in styrene. TEM images of the colloidal Si NCs samples prepared in the styrene solution of S1 (b) and S4 (c). Upper inset: HRTEM image of Si NCs; Lower inset: corresponding fast Fourier transform. The histograms of the colloidal Si NCs samples of S1 (d) and S4 (e) derived from the TEM images in (b) and (c), respectively. (f) The TEM image of the colloidal Si NCs of S4 with good dispersion three months later.

laser with a pulse width of 60 ps as the excitation source. The PL QYs of colloidal Si NCs in styrene solution were performed by using a Edinburgh FLS920 system under the excitation at 380 nm.

Figure 1(a) shows Raman spectra of S1–S4 prepared by the fs laser ablation in styrene solution. Owing to the first-order modes scatter at Brillouin zone center, a Raman active peak at around 520 cm^{-1} with the full width at half maximum (FWHM) of 3.4 cm^{-1} is found in the Raman spectrum of crystalline Si [26]. The Raman peaks of S1–S4 features at 519, 518, 517 and 516 cm^{-1}, and the corresponding FWHM is 11.3, 12.8, 14.5, and 15.5 cm^{-1}, respectively. The Raman peak positions of all the samples shift to smaller frequency in comparison with that of crystalline Si, together with widening FWHM, demonstrating the presence of ultrafine Si NCs [27]. It is generally accepted that phonon confinement model is considered as the main mechanism accounting for the observed size-dependent Raman characteristic. Crystal momentum keeps no longer conserved in small Si NCs, then phonon modes prefer in Si NCs rather than at the Brillouin zone center, giving rise to the phonon density of states, which results in downshift and broadening of the Raman peak [28]. The size-dependent characteristic of Raman peak position for Si NCs can be directly reflected by the phenomenological law [29]: $\Delta\omega = -19.856/d^{1.586}$. Where $\Delta\omega$ represents the value of downshift for Raman peak position of Si NCs with respect to that of crystalline Si, and d (in nm) is the average diameter of Si NCs. The average diameters for S1–S4 are 6.5, 4.5, 3.4, and 2.8 nm, respectively.

The representative TEM images for S1 and S4 are presented in figures 1(b) and (c), respectively. It can be seen that plenty of ultrafine nanoparticles are spherical and evenly dispersed on the grid without aggregation, indicating the successful passivation on the nanoparticle surfaces [30]. Estimated from the size distribution histograms, the average diameters of nanoparticles are ~6.5 and 2.7 nm for S1 and S4, respectively. With the increase of HF concentration, some oxidization layers at the surface of Si NCs can be etched effectively, and the Si–H bonds with weaker mechanical strength can be formed simultaneously [19]. Thus, the fragmentation of porous Si nanoparticles becomes easy, resulting in a great deal of small-sized Si NCs.

To better understand the structure of nanoparticles, HRTEM images for S1 and S4 are shown on the upper inset of figures 1(b) and (c), respectively. From the HRTEM images, we observe that the crystal lattice fringes with ~0.3 nm correspond to (111) plane of the Si crystals [31], and the etched particles keep their crystalline structure. The corresponding fast Fourier transform diffraction patterns of the HRTEM images are presented in the lower inset of figures 1(b) and (c), which indicates lattice spacing of 3.12 Å for the Si (111) planes [32]. It should be noted that the as-prepared colloidal Si NCs are quite stable. Three months later, the colloidal Si NCs still disperse very well without any

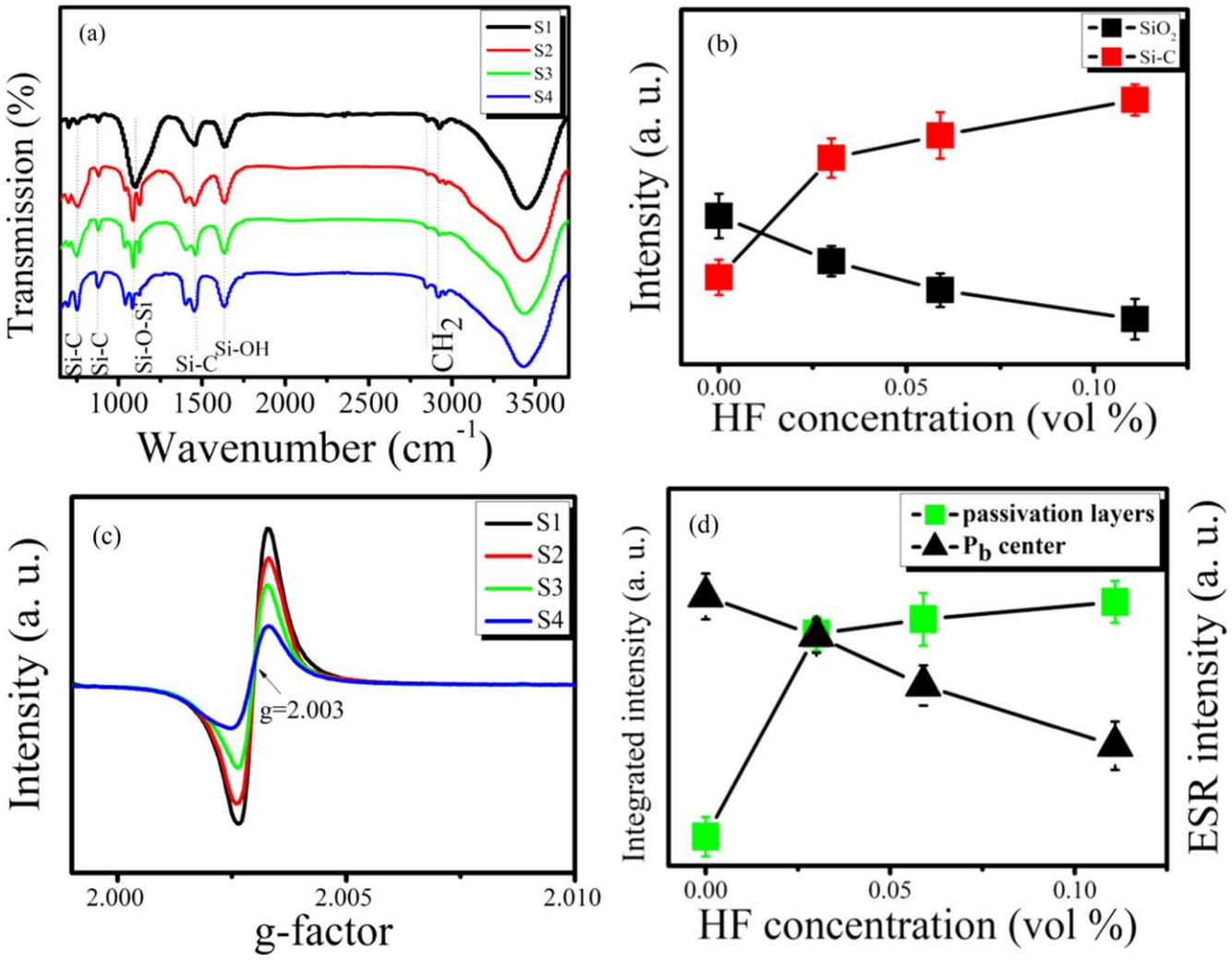

Figure 2. (a) FTIR spectra of the colloidal Si NCs samples prepared in the styrene solution for S1–S4. (b) The densities of SiO_2 and Si–C bonds (with error bars) as a function of HF concentration in styrene. (c) ESR signals measured for S1–S4. (d) Integrated passivation layers on the Si NCs surface and P_b center as a function of HF concentration in styrene (with error bars), respectively.

aggregation in solution, and the sizes of all the samples keep almost unchanged compared with the previous ones, as confirmed by the representative TEM image of S4 shown in figure 1(f).

Figure 2(a) displays the FTIR spectra of S1–S4 to identify and characterize the terminal bonding constructions on the surface of Si NCs. The clear absorption bands at around 753, 880, 1090, 1457, 1635, 2849, 2925 and 3432 cm^{-1} are ascribed to Si–C stretching vibration, Si–C symmetric vibration, Si–O–Si stretching, Si–CH_2 bending, Si–OH absorption, symmetric CH_2 stretching, antisymmetric CH_2 stretching and Si–OH absorption modes, respectively [17, 33–36]. It is demonstrated that the emergence of Si–O–Si bands confirms the formation of oxide layers passivation on the surface of prepared Si NCs via oxygen [18]. The presence of Si–C bands for all samples suggests that alkyl-related molecules have terminated the Si NCs surfaces [37]. The mechanisms of alkyl-related molecules passivation on Si NCs surface under fs Laser ablation in solution are interpreted by cycloaddition reaction, which has been demonstrated in our previous work [25].

Figure 2(b) shows the calculated intensities of the Si–O–Si and Si–C bonds by integrating the infrared absorption bands shown in figure 2(a). The intensities of Si–O–Si bending mode (1090 cm^{-1}) referring to the structural properties of SiO_2 decrease gradually with increasing HF concentration, implying that HF removes significant amount of surface dioxide layers of colloidal Si NCs [38]. Meanwhile, it is clear to find that the intensities of alkyl-related absorption bands (753, 880 and 1457 cm^{-1}) gradually enhance with increasing HF concentration. Two reasons are responsible for these increments. On one hand, adding HF to the samples' solution leads to the passivation by Si–H bands on the Si surfaces [19]. With increasing HF concentration, more and more Si–O–Si bonds can be substituted by Si–H bonds. More unstable Si–H bonds are decomposed and responded to unsaturated C=C doubles bonds of styrene molecules under laser ablation so that more alkyl-related bonds are joined on the Si NCs surface, giving rise to the increment of alkyl-related bonds intensities. On the other hand, the process of hydrosilylation and fs laser reaction induces sufficient fragmentation from the large sized Si NCs so that plenty of

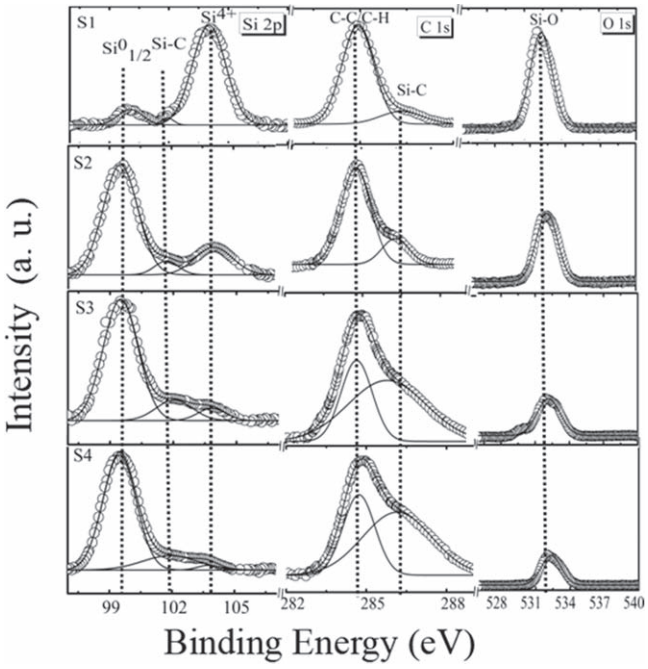

Figure 3. The experimental and fitting curves of Si2p, C1s and O 1s XPS spectra for S1–S4.

smaller sized Si NCs have more surfaces functional groups, resulting in the enhancement of the Si–C bonds intensities with increasing HF concentration [39]. The broad peak observed at 3432 cm^{-1} is ascribed to SiO–H or to moisture absorbed by the KBr pellet during the measurements [40].

Figure 2(c) shows the high-sensitivity ESR measurements of all samples to identify the signals of any paramagnetic defects. To get the calibration of ESR signal intensity and g factor, a Si:P marker sample was kept to be consistent with colloidal Si NCs sample for per-measurement [41]. The broad resonance at $g \approx 2.003$ is attributed to non-radiative recombination P_b centers, which originate from Si dangling bonds between the Si and SiO_2 interface regions [23]. In addition, no other signals from the SiO_2 specific centers E'_γ [42] and EX [43] which are often contributed to the blue emission in SiO_2 are observed [27, 41]. Figure 2(d) presents the densities of Si NCs surface passivation layers and ESR signals of P_b centers as a function of HF concentration, respectively. It is explicit that the densities of surface passivation layers increase while the P_b defect densities strongly decrease with increasing HF concentration. This indicates that the densities of dangling bonds between the Si and SiO_2 interface regions reduce gradually with increasing HF concentration.

To get further insight into the surface structures and passivation effect of colloidal Si NCs, XPS measurements of all samples were performed. Figure 3 presents the experimental and well-fitted Gaussian curves of Si 2p, C1s and O 1s spectra of S1–S4, respectively. The well-fitted Gaussian peaks at ~99.5, 101.9 and 103.7 eV in Si 2p spectra are attributed to bulk Si, Si–C and Si^{4+} species, respectively [44, 45]. The presence of Si–C in the 101.9 eV is deemed to be the charge trapping effect induced by fs irradiation for organically terminated Si NCs, the similar characteristic has been reported in [45]. The remaining of Si^{4+} indicates that there are some residual oxide overlayers on the surface of Si NCs. For the C 1s XPS spectra, it is clear to observe that two well-fitted Gaussian peaks locate at ~284.8 and 286.2 eV, respectively. The peak locates at 284.8 eV is ascribed to C–C and C–H bonds, and that at around 286.2 eV corresponds to Si–C bonds [46]. In the O 1s XPS spectra, there exists a peak at around 532.3 eV, corresponding to the Si–O bonds [47]. With increasing HF concentration, the O 1s peak intensity is observed to decrease gradually. The results of XPS spectra further demonstrate the well passivation on the Si NCs surface by alkyl-related molecules, as confirmed in FTIR results.

Based on previously reported procedures [25, 37], the amount of carbon chains on the surfaces of Si NCs is quantified as follows. Considering S4 as a representative, the calculated proportion of integrated region of Si 2p spectra to that of the Si–C bonding located at 286.2 eV in C 1s spectra is 4.6. On the basis of theoretical calculations [36], the amount of Si atoms for a pure Si NC with 2.37 nm average size is estimated to be 278. Hence, for each Si NC with an average size of 2.74 nm, there are totally 259 Si atoms in per Si NC as well as 56 Si–C bonds on the surfaces, and the number of Si atoms in surface layers is presumed to be approximately 86 [48]. Consequently, the value of surface carbon coverage is 65.1% for S4. Besides, the coverage on the Si NCs surface with carbon chains for S1–S3 is 33.7%, 48.8%, and 52.3%, respectively. The increment of surface coverage by carbon chains and the reduction of Si–O intensity are consistent with the results of FTIR.

UV–visible absorption spectra of the prepared colloidal Si NCs for S1–S4 are presented in figure 4(a). It is evident to observe that all absorption spectra have a distinctive shoulder at around 350 nm (~3.54 eV) together with a long absorption tail within the visible ranges. The shoulder at ~3.54 eV approaches to the direct transition at Γ-point (3.40 eV, $\Gamma_{25} \rightarrow \Gamma_{15}$) [49]. Meanwhile, the spectra are characterized by a blue-shift of the shoulder peak position from ~375 nm (~3.31 eV) in S1 to 325 nm (~3.82 eV) in S4 with increasing HF concentration. Owing to the effect of quantum confinement, the bandgap energy of Si NCs increases with reduction of their size as confirmed in Raman and TEM results, for which the absorption edge shifts to higher energy [50].

Another distinct feature of absorption spectra is that the absorbance ascends gradually with incremental HF concentration. Due to the fact that the investigated absorption light wavelength is much larger than the size of colloidal Si NCs, it is safely to neglect light scattering. Consequently, the absorbance ought to be proportional to the yield of fabricated Si NCs. Stronger absorption indicates that more Si nanoparticles can be acquired with increasing HF concentration. Thus, the higher concentration of solution are clearly expected from samples with increasing HF concentration.

Figure 4(b) shows the steady room temperature PL spectra of S1–S4 with excitation at 380 nm. A prominent emission band in the violet-blue range with double peaks at ~412 nm (3.01 eV) and 440 nm (2.82 eV) is clearly observed for all samples. Meanwhile, it is found that, with increasing

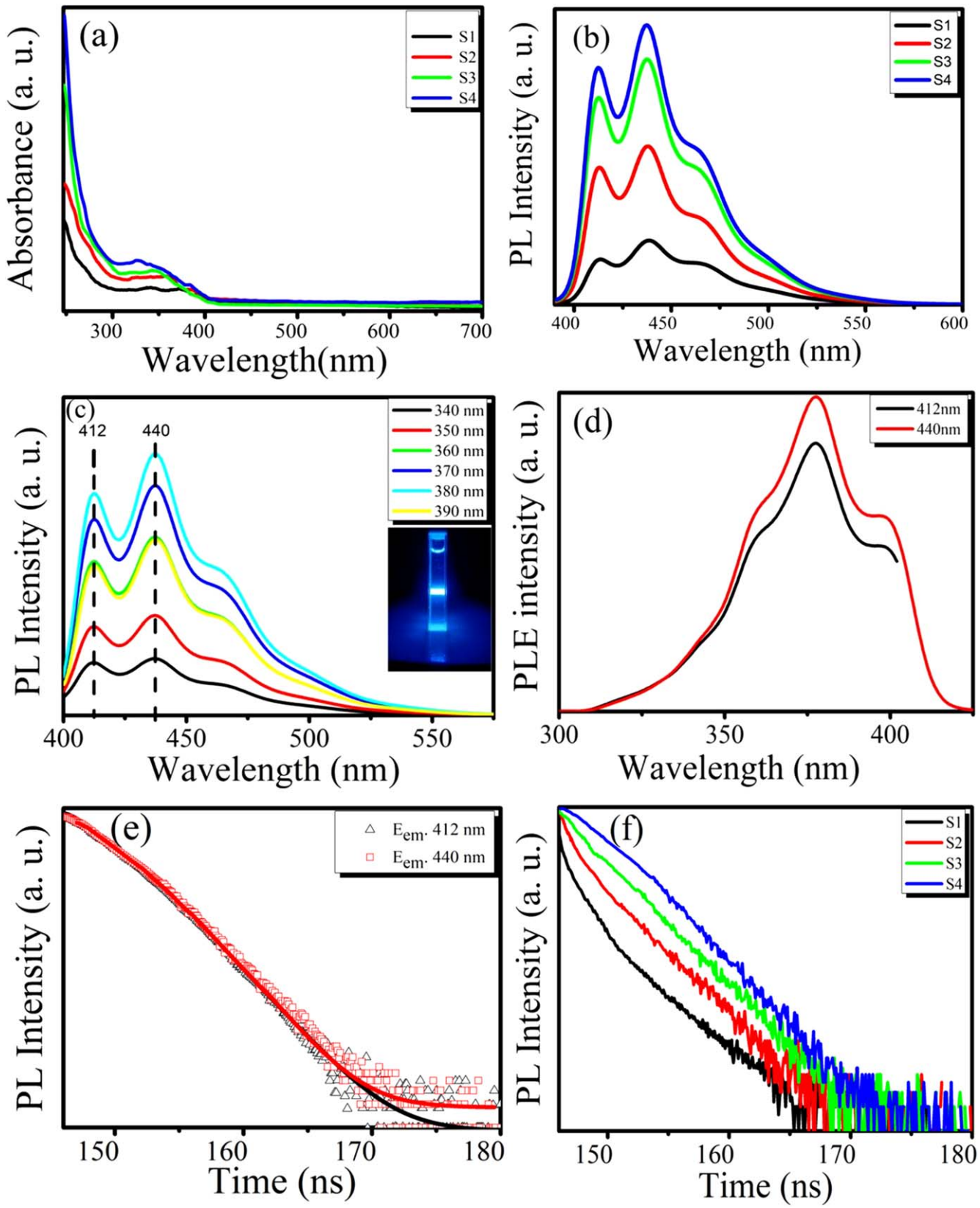

Figure 4. (a) UV–visible absorption spectra of the colloidal Si NCs samples prepared in the styrene solution for S1–S4. (b) The room temperature PL spectra with $\lambda_{exc} = 380$ nm for all samples. (c) Excitation and (d) emission spectra of S4. Inset: photograph of Si NCs dispersion for S4 under UV illumination. (e) PL decay curves of S4 detected at 412 and 440 nm, respectively. (f) PL decay curves of the colloidal Si NCs samples for S1–S4 in styrene detected at 440 nm.

HF concentration, the PL located at 412 nm (3.01 eV) keep unchanged as well as the peak at 440 nm (2.82 eV). The PL intensity tends to enhance remarkably with increasing HF concentration. It should be noted that there is no luminescence from styrene solution alone under illumination. This suggests that the double PL peaks are supposed to originate from colloidal Si NCs instead of styrene solution.

λ_{exc}-dependent PL, PLE and time-resolved PL measurements are performed for all samples so as to get further insight on the luminescence mechanism of blue PL. As a representative, figures 4(c) and (d) show the λ_{exc}-dependent PL and PLE spectra of S4, respectively. The PL peak positions at ~412 nm (3.01 eV) and 440 nm (2.82 eV) are invariable with increasing excitation wavelengths from 340 nm to 390 nm. The emission intensity increases gradually with increasing λ_{exc}, and reaches to the maximum luminescence intensity when is excited at $\lambda_{exc} = 380$ nm (3.26 eV), and then, the luminescence intensity shows dramatically reduction when the excitation wavelengths are over 380 nm. Figure 4(d) shows the PLE spectra of S4 with emission energies at $E_{em} = 412$ nm (3.01 eV) and 440 nm (2.82 eV), respectively. The obvious E_{PLE} value of peaks 380 nm (~3.26 eV) are found to be independent of detection wavelength, implying that the two PL peaks should originate from the same mechanism [51]. Moreover, the PLE intensities reach to the maximum values when the peak positions occur at 380 nm (~3.26 eV). It is rational to propose that the excitons absorb strongly at 380 nm (~3.26 eV) and radiative de-excitation occurs at 412 (3.01 eV) and 440 nm (2.82 eV) for colloidal Si NCs [52]. Figure 4(e) presents the experimental decay curves of S4 taken at 412 (hollow triangles) and 440 nm (red hollow squares) emission wavelengths along with the corresponding calculated (solid) curves, respectively. Decay curves can be well fitted with double-exponential iterative fitting program, where the model exponential function is [37]: $I(t) = A_1 e^{-t/\tau_1} + A_2 e^{-t/\tau_2}$. Here, I(t) is the intensity; A_1, A_2, τ_1, and τ_2 are the fitting constants. Fitting results show that for emission at 412 nm and 440 nm, $\tau_1 = 0.92$ ns ($A_1 = 68.7\%$), $\tau_1' = 8.23$ ns ($A_1' = 31.3\%$); $\tau_2 = 0.97$ ns ($A_2 = 69.3\%$) , $\tau_2' = 8.43$ ns ($A_2' = 30.7\%$), respectively. The mean lifetime $\overline{\tau}$ of colloidal Si NCs can be calculated by using following equation: $\overline{\tau} = (A_1\tau_1^{\,2} + A_2\tau_2^{\,2})/(A_1\tau_1 + A_2\tau_2)$. The obtained $\overline{\tau}$ for the emission at 412 nm and 440 nm are 6.78 ns and 6.89 ns, respectively. Figure 4(f) displays PL decay curves of S1–S4 detected at 440 nm. It is obtained that colloidal Si NCs possess featured lifetimes with a fast decay component from 0.43 to 0.97 ns and a slow one from 3.22 to 8.43 ns for S1–S4. The average lifetime $\overline{\tau}$ of colloidal Si NCs for S1–S4 are 2.27, 3.54, 5.24 and 6.89 ns, respectively. It is clear to find that the decay times for the colloidal Si NCs become longer with increasing HF concentration. According to the Marcus theory [53], the electron transfer rate K_{ET} can be described as:

$$K_{ET} = \frac{2\pi}{\hbar}\int_{-\infty}^{\infty} \rho(E)\ |\bar{H}(E)|^2 \frac{1}{\sqrt{4\pi\lambda k_B T}} \times \exp\left\{-\frac{(\lambda + \Delta G_0 + E)^2}{4\lambda k_B T}\right\}, \quad (1)$$

where $\Delta G_0 = E_{CB} - E(S^+/S^*)$ is free energy driving force, $\rho(E)$ density of accepting states, $\overline{H}(E)$ is the overlap matrix element, λ is the reorganizational energy, K_B is Boltzmann's constant, and T is absolute temperature. To simplify analysis in the theoretical model, $\overline{H}(E)$ is considered to be independent of energy. From the above theory, we find that transfer dynamics are dominated by the driving force and density of unoccupied electron accepting states. With increasing HF concentration, the sizes of the Si NCs reduce gradually so that the quantum confinement is enhanced, leading to the increment of conduction band edge and energy separation of the discrete states. Hence, the driving force and the attainment of the accepting states are expected to decrease [54]. Analyzing from the equation (1), we obtain a fact that a reduced electron transfer ratio is confirmed and thus the longer decay time is obtained with incremental HF concentration [54]. Based on first-principle calculations, nanosecond magnitudes of decay time for colloidal Si NCs is ascribed to the localized exciton transitions on the Si NCs surfaces, where the fast component correlates to the non-radiative excitons' trapping time on the localized states and the slow component corresponds to radiative and non-radiative recombination of the trapped excitons [55]. The decay time for fast component of colloidal Si NCs prolongs gradually with increasing HF concentration, indicating that non-radiative surface defect densities decrease gradually [56], in good agreement with ESR results.

We now focus on clarifying the PL mechanism of colloidal Si NCs. Due to quantum confinement effect, the energy of PL peak is supposed to red shift correspondingly when excitation wavelength shifts to longer wavelength. The PL peaks remain unchanged when excited by different wavelength from 340 nm to 390 nm, as shown in figure 4(c). Hence, it is affirmatively to eliminate the direct band-to-band recombination of electrons holes at Γ point. Analyzing from ESR spectra, we find that there is no other defect-related centers in SiO_2, therefore, the contribution of the SiO_2 component to the blue PL can be safely excluded as well. In this case, the alkyl-related bonds on the surface of colloidal Si NCs, as confirmed by FTIR and XPS spectra, is essential for the blue emission in the chemically modified samples. The alkyl-related radiative recombination centers have been introduced to initiate the blue emission [57]. We propose that the nature of the blue PL is most likely to originate from the following process: firstly, the excitons are excited at Γ point within Si NCs under excitation light irradiation. Subsequently, some excitons are caught by non-radiative P_b centers, while the rest of them transfer to surface related states (Si–C), and then radiative recombination takes place there, giving blue emissions at around 2.82 and 3.01 eV.

It has been reported that the PL intensity of Si NCs is restricted by P_b non-radiative recombination of excitons [58]. On the basis of the above analysis, we know that the process of trapping excitons by the P_b centers is suppressed, reflected by the decreasing numbers of P_b centers with incremental HF concentration. Meanwhile, the increasing alkyl-related radiative recombination centers dominate the emission process, leading to the enhancement of PL intensity.

To get further investigation of the optical characteristics, PL QYs measurements of the prepared colloidal Si NCs were carried out at room temperature. Before measurements, the

Table 1. Comparison about emission quantum yield of this work with various literature that have been reported by different research groups.

Group	Preparation of samples	Emission quantum yield(%)
Xin *et al* [17]	Si NCs conducted in different organic solvents by nanosecond laser	<10
Yuan *et al* [9]	The reversible transformation from Cl:Si NCs to carbon-terminated Si NCs (C:Si NCs) prepared via pulsed laser ablation	13
Nakamura *et al* [18]	Colloidal Si NCs prepared by laser irradiation	20–23
Limpens *et al* [23]	Si NCs prepared by sputtering and a high-temperature heat treatment	35
Miyano *et al* [19]	Si NCs under irradiation UV light at 365 nm with HF	55
Mangolini *et al* [20, 21]	Nonthermal plasmas, wet-chemical surface passivation with organic ligands	60–70
Li *et al* [22]	Ultrabright Si nanoparticles fabricated through designed chemical surface modification	75
This work	Si NCs under fs laser in organic solution with HF	76.5

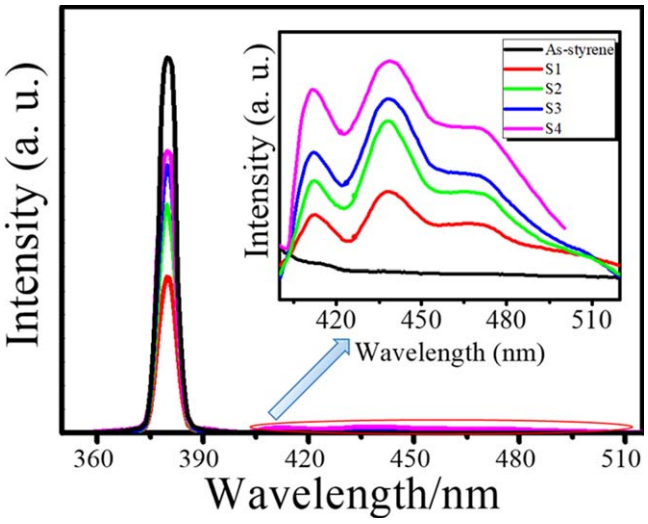

Figure 5. Emission quantum yields of S1–S4 under excitation at 380 nm. Inset: the much clearer luminescence spectra of S1 ∼ S4 samples.

spectral were strictly calibrated according to [59]. After finishing measurements, the luminescence spectra were carefully integrated using the 'Origin' Microsoft, which is the most frequently used to process the data.

Figure 5 presents the PL QYs of S1–S4. The peak centered at 380 nm is formed by the absorption of the excited light by the pure reference styrene solution (black curve) and target samples (colorful curves), respectively, that is, the excitation beam which has been absorbed. The value of PL QY is defined as the ratio of emitted photons to the absorbed ones, which is reflected by the following equation:

$$\mathrm{QY} = \frac{N_{\mathrm{em}}}{N_{\mathrm{abs}}} = \frac{N_{\mathrm{em}}}{N_{\mathrm{blank}} - N_{\mathrm{sample}}}, \tag{2}$$

where N_{em} stands for the integrated spectra of the sample's luminescence wavelength range (∼400–500 nm), as seen in the inset of figure 5. N_{abs} means the total amount of absorbed photons. N_{blank} and N_{sample} represent the as-styrene and sample's integrated spectra of excitation beam (see sharp spectra in figure (5)), respectively. A cuvette filled with pure styrene solution was used as the blank for each measurements of samples [60]. The calculated results are 16.3%, 26.1%, 53.9% and 76.5% for S1–S4, respectively. The maximum PL QY of S4 is obviously larger than previous reports for Si NCs (see table 1). To investigate the enhancement of PL QYs with increasing HF concentration, one reason with respect to the radiative and non-radiative recombination procedure is taken into account as follows [17, 61]:

$$\mathrm{QY} = \frac{k_r}{k_r + k_{nr}}, \tag{3}$$

$$\tau_{ave} = \frac{1}{k_r + k_{nr}}, \tag{4}$$

where k_r, k_{nr} and τ_{ave} are the radiative, non-radiative recombination rates and average lifetime, respectively. As confirmed from the PL decay curve, τ_{ave} becomes longer from 2.27 to 6.89 ns for S1–S4, the calculated k_r from equations (3) and (4) increases from $7.1 \times 10^7\ \mathrm{s}^{-1}$ to $11.3 \times 10^7\ \mathrm{s}^{-1}$ for S1–S4, and k_{nr} decreases from $36.4 \times 10^8\ \mathrm{s}^{-1}$ to $3.5 \times 10^7\ \mathrm{s}^{-1}$ for S1–S4. The values of k_r and k_{nr} near $10^7\ \mathrm{s}^{-1}$ are consistent with that of blue PL from alkyl-terminated Si NCs [15]. Moreover, the calculated results of the reduction in non-radiative recombination rates are in good agreement with ESR results, which reveals that the enhancement of surface passivation of Si NCs through alkyl-related bonds leads to the reduction of Si dangling bonds and further results in the decrease of non-radiative recombination rate. Furthermore, the alkyl-related radiative recombination centers are introduced to increase, leading to the enhancement of radiative recombination rate. Thus, the reduction of k_{nr} and the increase of k_r contribute to the effective enhancement of PL QYs.

The other reason accounting for the increment of PL QYs is that adding HF to the styrene solution can effectively promote the hydrosilylation process and the photo-initiated reaction, the radiative recombination process can be thus enhanced by increasing alkyl-related passivation. From the results of UV–vis absorption spectra, it can be concluded that more Si nanoparticles are obtained, indicating that the yield of Si NCs enhances with increasing HF concentration.

In conclusion, we have investigated the structural transformation, PL properties, and significant improvement of fluorescence quantum yield for colloidal Si NCs by fs laser ablation in styrene containing incremental concentration of

HF from 0 to 11.1 vol%. With increasing HF concentration, the decreasingly average size from 6.5 to 2.7 nm, the enhancement of Si NCs surface passivation with alkyl-related molecules and the reduction in the densities of dangling bonds between Si/SiO_2 interface regions are revealed by Raman scattering, HRTEM, FTIR, XPS, and ESR measurements. It is shown that adding HF to the styrene solution is found to remove the dioxide layers and then replace them by alkyl-related bonds under fs laser ablation, leading to the lower defect density of non-radiative P_b defect centers. In accordance with the structural characterizations, UV–vis absorption, PLE spectra, and time-resolved PL, we propose that the blue emissions from colloidal Si NCs originate from the following process: under excitation light irradiation, the excitons are excited at Γ point within Si NCs, and then, some excitons are caught by non-radiative P_b centers, while the rest of them transfer to alkyl-related radiative recombination centers and emit blue PL at around 2.82 and 3.01 eV. The effective passivation and the suppression of non-radiative P_b centers lead to the enhancement of PL QYs from 16.3% to 76.5% with incremental HF concentration from 0 to 11.1 vol%. Addition of HF to the styrene solution for fabricating colloidal Si NCs by fs laser ablation is considered as an effective approach to promote hydrosilylation and the photo-initiated reaction.

Acknowledgments

The authors thank the National Natural Science Foundation of China for the support. This work was financially supported by the National Natural Science Foundations of China (Grant Nos. 11504229 and 61234005), and Shanghai University of Engineering Science ESI Fund (ESI201809) and Innovation Fund for Graduate Students (17KY0512).

Conflicts of interest

There are no conflicts of interest to declare.

ORCID iDs

Huilian Hao https://orcid.org/0000-0001-5446-5071

References

[1] Canham L T 1990 Silicon quantum wire array fabrication by electrochemical and chemical dissolution of wafers *Appl. Phys. Lett.* **57** 1046–8

[2] Balci M H, Aas L M S, Kildemo M, Sæterli R, Holmestad R, Lindgren M, Grande T and Einarsrud M A 2016 White light emitting silicon nano-crystals-polymeric hybrid films prepared by single batch solution based method *Thin Solid Films* **603** 126–33

[3] Ni Z Y, Ma L L, Du S C, Xu Y, Yuan M, Fang H H, Wang Z, Xu M S, Li D S and Yang J Y 2017 Plasmonic silicon quantum dots enabled high-sensitivity ultra-broadband photodetection of graphene-based hybrid phototransistors *ACS Nano* **11** 9854–62

[4] Liu X K, Zhao S Y, Gu W, Zhang Y T, Qiao X S, Ni Z Y, Pi X D and Yang D R 2018 Light-emitting diodes based on colloidal silicon quantum dots with octyl and phenylpropyl ligands *ACS Appl. Mater. Interfaces* **10** 5959–66

[5] Zhao S Y, Pi X D, Mercier C, Yuan Z C, Sun B Q and Yang D R 2016 Silicon-nanocrystal-incorporated ternary hybrid solar cells *Nano Energy* **26** 305–12

[6] Mcvey B F P, Prabakar S, Gooding J J and Tilley R D 2017 Solution synthesis, surface passivation, optical properties, biomedical applications, and cytotoxicity of silicon and germanium nanocrystals *ChemPlusChem* **82** 60–73

[7] Yang Z, Reyes G B D L, Titova L V, Sychugov I, Dasog M, Linnros J, Hegmann F A and Veinot J G C 2015 Evolution of the ultrafast photoluminescence of colloidal silicon nanocrystals with changing surface chemistry *ACS Photonics* **2** 595–605

[8] Hanrahan M P, Fought E L, Windus T L, Wheeler L M, Anderson N C, Neale N R and Rossini A J 2017 Characterization of silicon nanocrystal surfaces by multidimensional solid-state NMR spectroscopy *Chem. Mater.* **29** 10339–51

[9] Yuan Z, Nakamura T, Adachi S and Matsuishi K 2016 Luminescence color control and quantum-efficiency enhancement of colloidal Si nanocrystals by pulsed laser irradiation in liquid *Nanoscale* **9** 1193–200

[10] Chen T, Skinner B, Xie W, Shklovskii B I and Kortshagen U R 2014 Carrier transport in films of alkyl-ligand-terminated silicon nanocrystals *J. Phys. Chem.* C **118** 19580–8

[11] Yang Z, Dasog M and Dobbie A R 2014 Hybrid materials: highly luminescent covalently linked silicon nanocrystal/polystyrene hybrid functional materials: synthesis, properties, and processability *Adv. Funct. Mater.* **24** 1345–53

[12] Hua F, Swihart M T and Ruckenstein E 2012 Efficient surface grafting of luminescent silicon quantum dots by photoinitiated hydrosilylation *Langmuir* **21** 6054–62

[13] Schäfer J, Fricke K, Mika F, Pokorná Z, Zajíčková L and Foest R 2016 Liquid assisted plasma enhanced chemical vapour deposition with a non-thermal plasma jet at atmospheric pressure *Thin Solid Films* **630** 71–8

[14] Xiao J J, Qiu Z M, Yang W R, Qiu J M, Yang T L, Xu Y D, Zeng Y J, Wang F C and Li S K 2018 Organosilicone modification of allyl methacrylate with speier's catalyst for waterborne self-matting styrene-acrylic emulsion *Prog. Org. Coat.* **116** 1–6

[15] Dohnalová K, Poddubny A N, Prokofiev A A, Boer W D D, Umesh C P, Paulusse J M, Han Z and Gregorkiewicz T 2013 Surface brightens up Si quantum dots: direct bandgap-like size-tunable emission *Light: Sci. Appl.* **2** e47

[16] Shirahata N, Hirakawa D and Sakka Y 2010 Interfacial-related color tuning of colloidal Si nanocrystals *Green Chem.* **12** 2139–41

[17] Xin Y, Kitasako T, Maeda M and Saitow K I 2017 Solvent dependence of laser-synthesized blue-emitting Si nanoparticles: size, quantum yield, and aging performance *Chem. Phys. Lett.* **674** 90–7

[18] Nakamura T, Yuan Z, Watanabe K and Adachi S 2016 Bright and multicolor luminescent colloidal Si nanocrystals prepared by pulsed laser irradiation in liquid *Appl. Phys. Lett.* **108** 023105

[19] Miyano M, Endo S, Takenouchi H, Nakamura S, Iwabuti Y, Shiino O, Nakanishi T and Hasegawa Y 2014 Novel synthesis and effective surface protection of air-stable luminescent silicon nanoparticles *J. Phys. Chem.* C **118** 19778–84

[20] Mangolini L, Jurbergs D, Rogojina E and Kortshagen U 2010 High efficiency photoluminescence from silicon nanocrystals prepared by plasma synthesis and organic surface passivation *Phys. Status Solidi* **3** 3975–8

[21] Jurbergs D, Rogojina E, Mangolini L and Kortshagen U 2006 Silicon nanocrystals with ensemble quantum yields exceeding 60% *Appl. Phys. Lett.* **88** 2915

[22] Li Q, He Y, Chang J, Wang L, Chen H Z, Tan Y W, Wang H Y and Shao Z Z 2013 Surface-modified silicon nanoparticles with ultrabright photoluminescence and single-exponential decay for nanoscale fluorescence lifetime imaging of temperature *J. Am. Chem. Soc.* **135** 14924–7

[23] Limpens R, Luxembourg S L, Weeber A W and Gregorkiewicz T 2016 Emission efficiency limit of Si nanocrystals *Sci. Rep.* **6** 19566

[24] Zhang Y X, Wu W S, Hao H L and Shen W Z 2018 Femtosecond laser-induced size reduction and emission quantum yield enhancement of colloidal silicon nanocrystals: effect of laser ablation time *Nanotechnology* **29** 365706

[25] Wu W S, Hao H L, Zhang Y X, Li J, Wang J J and Shen W Z 2018 Correlation between luminescence and structural evolution of colloidal silicon nanocrystals synthesized under different laser fluences *Nanotechnology* **29** 025709

[26] Kuzmin P G, Shafeev G A, Bukin V V, Garnov S V, Farcau C, Carles R, Warotfontrose B, Guieu V and Viau G 2010 Silicon nanoparticles produced by femtosecond laser ablation in ethanol: size control, structural characterization, and optical properties *J. Phys. Chem.* C **114** 15266–73

[27] Yang S K, Li W Z, Cao B Q, Zeng H B and Cai W P 2011 Origin of blue emission from silicon nanoparticles: direct transition and interface recombination *J. Phys. Chem.* C **115** 21056–62

[28] Hessel C M, Wei J, Reid D, Fujii H, Downer M C and Korgel B A 2012 Raman spectroscopy of oxide-embedded and ligand-stabilized silicon nanocrystals *J. Phys. Chem. Lett.* **3** 1089–93

[29] Vaccaro L, Sciortino L, Messina F, Buscarino G, Agnello S and Cannas M 2014 Luminescent silicon nanocrystals produced by near-infrared nanosecond pulsed laser ablation in water *Appl. Surf. Sci.* **302** 62–5

[30] Zou J and Kauzlarich S M 2008 Functionalization of silicon nanoparticles via silanization: alkyl, halide and ester *J. Cluster Sci.* **19** 341–55

[31] Nakamura T, Yuan Z and Adachi S 2014 High-yield preparation of blue-emitting colloidal Si nanocrystals by selective laser ablation of porous silicon in liquid *Nanotechnology* **25** 275602

[32] Intartaglia R, Bagga K, Brandi F, Das G, Genovese A, Fabrizio E D and Diaspro A 2011 Optical properties of femtosecond laser-synthesized silicon nanoparticles in deionized water *J. Phys. Chem.* C **115** 5102–7

[33] Xu D, Sun L, Li H, Zhang L, Guo G, Zhao X and Gui L 2003 Hydrolysis and silanization of the hydrosilicon surface of freshly prepared porous silicon by an amine catalytic reaction *New J. Chem.* **27** 300–6

[34] Mardanian M, Tarasenko N V and Nevar A A 2014 Influence of liquid medium on optical characteristics of the Si nanoparticles prepared by submerged electrical spark discharge *Braz. J. Phys.* **44** 240–6

[35] Mariotti D, Svrcek V, Hamilton J W J, Schmidt M and Kondo M 2012 Silicon nanocrystals in liquid media: optical properties and surface stabilization by microplasma-induced non-equilibrium liquid chemistry *Adv. Funct. Mater.* **22** 954–64

[36] Rosso-Vasic M, Spruijt E, Van Lagen B, De Cola L and Zuilhof H 2008 Alkyl-functionalized oxide-free silicon nanoparticles: synthesis and optical properties *Small* **5** 1835–41

[37] Tan D Z, Ma Z J, Xu B B, Dai Y, Ma G H, He M, Jin Z M and Qiu J R 2011 Surface passivated silicon nanocrystals with stable luminescence synthesized by femtosecond laser ablation in solution *Phys. Chem. Chem. Phys.* **13** 20255–61

[38] Chou J S and Lee S C 1995 Effect of porosity on infrared-absorption spectra of silicon dioxide *J. Appl. Phys.* **77** 1805–7

[39] Nguyen V, Yan L, Si J and Hou X 2015 Femtosecond laser-induced size reduction of carbon nanodots in solution: effect of laser fluence, spot size, and irradiation time *J. Appl. Phys.* **117** 084304

[40] Li X G, He Y Q and MT S 2004 Surface functionalization of silicon nanoparticles produced by laser-driven pyrolysis of silane followed by HF-HNO_3 etching *Langmuir* **20** 4720–7

[41] Godefroo S, Hayne M, Jivanescu M, Stesmans A, Zacharias M, Lebedev O I, Van Tendeloo G and Moshchalkov V V 2008 Classification and control of the origin of photoluminescence from Si nanocrystals *Nat. Nanotechnol.* **3** 174–8

[42] Warren W L, Kanicki J, Rong F C and Poindexter E H 1992 Paramagnetic point defects in amorphous silicon dioxide and amorphous silicon nitride thin films *J. Electrochem. Soc.* **139** 872–80

[43] Stesmans A and Scheerlinck F 1994 Natural intrinsic EX center in thermal SiO_2 on Si: ^{17}O hyperfine interaction *Phys. Rev.* B **50** 5204–12

[44] Yu Y and Korgel B A 2015 Controlled styrene monolayer capping of silicon nanocrystals by room temperature hydrosilylation *Langmuir* **31** 6532–7

[45] Dung M X, Choi J K and Jeong H D 2013 Newly synthesized silicon quantum dot-polystyrene nanocomposite having thermally robust positive charge trapping *ACS Appl. Mater. Interfaces* **5** 2400–9

[46] Wang Q, Ni H J, Pietzsch A, Hennies F, Bao Y P and Chao Y M 2011 Synthesis of water-dispersible photoluminescent silicon nanoparticles and their use in biological fluorescent imaging *J. Nanopart. Res.* **13** 405–13

[47] Jo M H, Park H H, Kim D J, Hyun S H, Choi S Y and Paik J T 1997 SiO_2 aerogel film as a novel intermetal dielectric *J. Appl. Phys.* **82** 1299–304

[48] Hao H L, Wu W S, Zhang Y, Wu L K and Shen W Z 2016 Origin of blue photoluminescence from colloidal silicon nanocrystals fabricated by femtosecond laser ablation in solution *Nanotechnology* **27** 325702

[49] Wilcoxon J P, Samara G A and Provencio P N 1999 Optical and electronic properties of Si nanoclusters synthesized in inverse micelles *Phys. Rev.* B **60** 2704–14

[50] Shirahata N 2011 Colloidal Si nanocrystals: a controlled organic-inorganic interface and its implications of color-tuning and chemical design toward sophisticated architectures *Phys. Chem. Chem. Phys.* **13** 7284–94

[51] Yang S, Cai W, Zeng H and Li Z 2008 Polycrystalline Si nanoparticles and their strong aging enhancement of blue photoluminescence *J. Appl. Phys.* **104** 023516

[52] Chaturvedi A, Joshi M P, Rani E, Ingale A, Srivastava A K and Kukreja L M 2014 On red-shift of UV photoluminescence with decreasing size of silicon nanoparticles embedded in SiO_2 matrix grown by pulsed laser deposition *J. Lumin.* **154** 178–84

[53] Tvrdy K, Frantsuzov P A and Kamat P V 2011 Photoinduced electron transfer from semiconductor quantum dots to metal oxide nanoparticles *Proc. Natl Acad. Sci. USA* **108** 29–34

[54] Wen X M, Zhang P F, Smith T A, Anthony R J, Kortshagen U R, Yu P, Feng Y, Shrestha S, Coniber G and Huang S J 2015 Tunability limit of photoluminescence in colloidal silicon nanocrystals *Sci. Rep.* **5** 12469

[55] Hao H L and Shen W Z 2008 Identification and control of the origin of photoluminescence from silicon quantum dots *Nanotechnology* **19** 455704

[56] Yuan Z, Nakamura T, Adachi S and Matsuishi K 2017 Improvement of laser processing for colloidal silicon nanocrystal formation in a reactive solvent *J. Phys. Chem.* C **121** 8623–9

[57] Li H, Xu D, Guo G, Gui L, Tang Y, Ai X, Sun Z, Zhang X and Qin G G 2000 Intense and stable blue-violet emission from porous silicon modified with alkyls *J. Appl. Phys.* **88** 4446–8

[58] Gupta A and Wiggers H 2011 Freestanding silicon quantum dots: origin of red and blue luminescence *Nanotechnology* **22** 055707

[59] Valenta J 2014 Determination of absolute quantum yields of luminescing nanomaterials over a broad spectral range: from the integrating sphere theory to the correct methodology *Nanosci. Methods* **3** 11–27

[60] Chung N X, Limpens R and Gregorkiewicz T 2017 Photoluminescence quantum yield in ensembles of Si nanocrystals *Adv. Opt. Mater.* **5** 1600709

[61] Sillen A and Engelborghs Y 2010 The correct use of 'average' fluorescence parameters *Photochem. Photobiol.* **67** 475–86